



A comparison of satellite observations with the XCO₂ surface obtained by fusing TCCON measurements and GEOS-Chem model outputs



Li Li Zhang^{a,b,c}, Tian Xiang Yue^{a,b,*}, John P. Wilson^{a,b,d}, Na Zhao^{a,b}, Ya Peng Zhao^e, Zheng Ping Du^{a,b}, Yu Liu^{a,b}

^a State Key Laboratory of Resources and Environment Information System, Institute of Geographical Sciences and Natural Resources Research, Chinese Academy of Sciences, Beijing 100101, China

^b College of Resources and Environment, University of Chinese Academy of Sciences, Beijing 100049, China

^c Institute of Remote Sensing and Digital Earth, Chinese Academy of Sciences, Beijing 100101, China

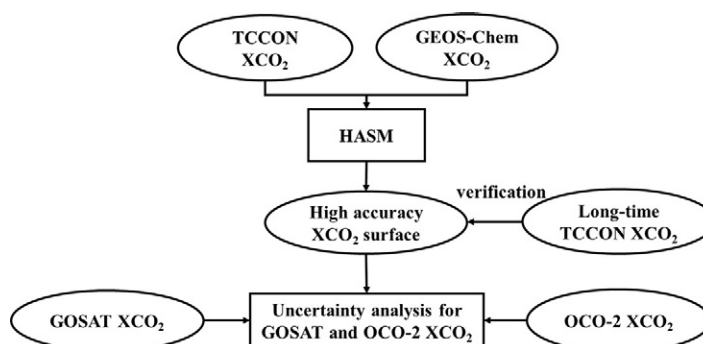
^d Spatial Sciences Institute, Dana and David Dornsife College of Letters, Arts, and Sciences, University of Southern California, Los Angeles, CA 90089-0374, USA

^e College of Computer Science and Engineering, Shandong University of Science and Technology, Qingdao 266590, China

HIGHLIGHTS

- HASM is used to model continuous XCO₂ surface taking TCCON observations as its optimum control constraints and GEOS-Chem as its driving field.
- Long-time TCCON data is used to verify high accuracy XCO₂ surface.
- High accuracy XCO₂ surface is used to evaluate satellites observations' uncertainty.

GRAPHICAL ABSTRACT



ARTICLE INFO

Article history:

Received 12 March 2017

Received in revised form 7 May 2017

Accepted 2 June 2017

Available online 9 June 2017

Editor: D. Barcelo

Keywords:

XCO₂ evaluation
 HASM method
 GEOS-Chem model
 TCCON observations
 Satellites observations

ABSTRACT

Ground observations can capture CO₂ concentrations accurately but the number of available TCCON (Total Carbon Column Observing Network) sites is too small to support a comprehensive analysis (i.e. validation) of satellite observations. Atmospheric transport models can provide continuous atmospheric CO₂ concentrations in space and time, but some information is difficult to generate with model simulations. The HASM platform can model continuous column-averaged CO₂ dry air mole fraction (XCO₂) surface taking TCCON observations as its optimum control constraints and an atmospheric transport model as its driving field. This article presents a comparison of the satellite observations with a HASM XCO₂ surface obtained by fusing TCCON measurements with GEOS-Chem model results. We first verified the accuracy of the HASM XCO₂ surface using six years (2010–2015) of TCCON observations and the GEOS-Chem model XCO₂ results. The validation results show that the largest MAE of bias between the HASM results and observations was 0.85 ppm and the smallest MAE was only 0.39 ppm. Next, we modeled the HASM XCO₂ surface by fusing the TCCON measurements and GEOS-Chem XCO₂ model results for the period 9/1/14 to 8/31/15. Finally, we compared the GOSAT and OCO-2 observations with the HASM XCO₂ surface and found that the global OCO-2 XCO₂ estimates more closely resembled the HASM XCO₂ surface than the GOSAT XCO₂ estimates.

© 2017 Elsevier B.V. All rights reserved.

* Corresponding author at: State Key Laboratory of Resources and Environment Information System, Institute of Geographical Sciences and Natural Resources Research, Chinese Academy of Sciences, Beijing 100101, China.

E-mail addresses: zhangll@reis.ac.cn (L.L. Zhang), yue@reis.ac.cn (T.X. Yue).

1. Introduction

Anthropogenic greenhouse gas emissions led by CO₂ have increased dramatically since the pre-industrial period and grew 2.0 ± 0.1 ppm/year for period 2002–2011 (IPCC, 2014).

The global monitoring of CO₂ from space at high spatiotemporal resolution is supposed to deepen our knowledge of the seasonal cycles of carbon sources, sinks and their global distribution (Rayner and O'Brien, 2001; Chevallier et al., 2007, 2009; Yoshida et al., 2011, 2012; Yue et al., 2016). The SCIAMACHY (Scanning Imaging Absorption Spectrometer for Atmospheric Cartography) instrument on ENVISAT (March 2002–April 2012) was the first satellite instrument to gather shortwave infrared (SWIR) and near-infrared (NIR) measurements of XCO₂ (Burrows et al., 1995; Bovensmann et al., 1999). There are three satellites orbiting the Earth that measure reflected solar radiation and support the retrieval of XCO₂ in the near infrared spectral region: the GOSAT (Kuze et al., 2009; Yoshida et al., 2011), OCO-2 (Crisp et al., 2004; Boesch et al., 2011), and TanSat (Liu et al., 2014; Liu and Yang, 2016; Zhang et al., 2016) satellites launched in April 2009, July 2014, and December 2016, respectively.

We need to evaluate qualities of these satellite observations. Ground-based measurements have been widely used to evaluate satellite observations (e.g. Bosch et al., 2006; Reuter et al., 2011; Yoshida et al., 2013; Lei et al., 2014; Zhao et al., 2017). The network of ground-based Fourier Transform Spectrometers, TCCON (Wunch et al., 2011), records direct solar spectra within the near-infrared spectral region where accurate and precise XCO₂ are retrieved. TCCON provides a limited but valuable resource for validating the satellite observations given the relatively low number of stations and their locations far away from anthropogenic emission sources and human activity (Lei et al., 2014). Atmospheric transport models, such as the GEOS-Chem (Bey et al., 2001; Suntharalingam et al., 2004; Baker et al., 2006) global 3-D chemical transport model for atmospheric composition driven by meteorological inputs, have also played a valuable role in the study of atmospheric CO₂ concentrations (Barkley et al., 2006; Reuter et al., 2011; Shim et al., 2011; Lei et al., 2014; Belikov et al., 2014). These models have limitations as well and in one such study, Feng et al. (2011) showed that model simulated CO₂ columns could not reproduce the magnitude of the minima during the growing season.

Ground observation makes it possible to obtain accurate data; however, regional observations are too sparse to validate satellite observations that offer global coverage. Model simulation results can obtain spatially continuous earth surface information, but some detailed information is difficult to gather from model simulations. The HASM (Yue, 2011; Yue et al., 2015) platform uses the fundamental theorem of surfaces to solve of earth surface modeling problems. One surface is uniquely defined by the first fundamental coefficients describing details of the surface observed when we are on the surface, while the second describes the change of the surface observed from outside (Henderson, 1998). The global approximate results simulated by the model are regarded as the driving field by HASM and locally accurate ground observation data is considered as the optimum control constraints. HASM can take full advantage of the GEOS-Chem model simulations and TCCON observations to simulate a high accuracy and continuous XCO₂ surface, which can then be deployed and used to understand and characterize the uncertainties of the XCO₂ satellite observations.

That said, the remainder of the article is structured as follows. Section 2 explains the materials and methods used for the study, including the GOSAT, OCO-2, and TCCON XCO₂ observations, the GEOS-Chem model, the HASM method and experimental workflow. Section 3 first verifies the HASM method and then uses it to model the XCO₂ surface with high accuracy and evaluate the efficacy of the GOSAT and OCO-2 XCO₂ observations. And Section 4 provides a discussion of the results, concludes the article and discusses future work.

Table 1

GOSAT L2 XCO₂ readings from 9/1/14 to 8/31/15.

		GOSAT XCO ₂				
		Number	Min (ppm)	Max (ppm)	Mean (ppm)	Std (ppm)
2014	September	22,205	376.23	406.23	394.13	2.24
	October	7748	376.23	402.50	394.11	1.96
	November	6907	386.96	406.23	394.85	2.19
	December	11,771	387.33	411.05	395.96	3.07
2015	January	–	–	–	–	–
	February	8685	387.33	411.05	396.11	3.09
	March	21,782	370.49	414.68	397.54	2.95
	April	6372	370.49	414.68	397.80	2.92
	May	7365	389.99	410.00	398.31	2.81
	June	26,375	382.49	409.83	396.32	2.80
	July	9290	383.01	409.17	396.02	2.88
	August	9153	382.49	409.83	395.89	2.83

2. Materials and methods

We evaluated the GOSAT and OCO-2 satellite observations from 9/1/14 to 8/31/15 using a high accuracy XCO₂ surface. We used HASM to simulate the high accuracy XCO₂ surface (HASM XCO₂), taking the GEOS-Chem model results (GEOS-Chem XCO₂) as the driving field and TCCON measurements (TCCON XCO₂) as the optimum control constraints. We then compared the GOSAT and OCO-2 measurements (GOSAT XCO₂ and OCO-2 XCO₂) with the HASM XCO₂ surface to analyze the global monthly and annual bias distributions and assess the efficacy of using these satellite observations to monitor XCO₂ across different continents, latitude and longitude zones.

2.1. GOSAT XCO₂

GOSAT was jointly developed by the Japanese Ministry of the Environment, National Institute for Environmental Studies, and Japan Aerospace Exploration Agency to monitor global distributions of CO₂ and CH₄ (methane). GOSAT was placed in a sun-synchronous orbit with 3-day recurrence at an altitude of 666 km and descending node around 12:48 local time equipped with the TANSO-FTS (the Thermal and Near infrared Sensor for carbon Observation-Fourier Transform Spectrometer) and TANSO-CAI (the Cloud and Aerosol Imager) instruments (Kuze et al., 2009).

Measuring solar light reflected from the Earth's surface in the short-wave infrared region (centered at 0.76, 1.6 and 2.0 μm) with two orthogonal linear polarizations that are designated as "P" and "S", TANSO-FTS also receives thermal radiation from the thermal infrared region (5.5 to 14.3 μm). With the repeating 3-day orbital cycle, GOSAT observes the spectra using single soundings and a footprint that measures 10.5 km on a side. Column-averaged dry-air fractions of CO₂

Table 2

OCO-2 L2 XCO₂ readings from 9/1/14 to 8/31/15.

		OCO-2 XCO ₂				
		Number	Min (ppm)	Max (ppm)	Mean (ppm)	Std (ppm)
2014	September	250,414	387.42	401.30	395.77	1.02
	October	34,356	391.60	401.01	395.53	0.89
	November	107,061	387.42	401.30	396.03	0.78
	December	380,597	390.13	403.80	396.45	0.84
2015	January	89,219	390.67	402.23	396.48	0.76
	February	147,529	390.13	403.02	396.34	0.96
	March	178,943	390.66	405.82	397.07	1.38
	April	47,624	392.88	404.49	397.31	1.38
	May	16,254	393.65	405.82	398.45	1.50
	June	73,722	388.68	405.83	398.59	1.55
	July	24,319	388.68	404.52	398.54	1.51
	August	28,152	390.42	405.83	398.18	1.41



Fig. 1. Distribution of TCCON sites (<https://tcon-wiki.caltech.edu/Sites>).

Table 3
TCCON site details.

Number	Sites	Starting date	Latitude (°)	Longitude (°)	Latitude (km)
1	Anmyeondo, Korea	Aug-2014	36.5382N	126.3311E	0.030
2	Ascension Island	May-2012	7.9165S	14.3325W	0.01
3	Bialystok, Poland	Mar-2009	53.23N	23.025E	0.18
4	Bremen, Germany	Jul-04	53.10N	8.85E	0.027
5	Pasadena/Caltech, USA	Sep-2012	34.136N	118.127W	0.230
6	Darwin, Australia	Jul-2015	12.45606S	130.92658E	0.037
7	Edwards/Dryden, USA	Jul-2013	34.958N	117.882W	0.699
8	Eureka, Canada	Aug-2006	80.05N	86.42W	0.61
9	Garmisch, Germany	Jul-2007	47.476N	11.063E	0.74
10	Izana, Tenerife	May-2007	28.3N	16.5W	2.37
11	Karlsruhe, Germany	Sep-2009	49.100N	8.439E	0.116
12	Lamont, USA	Jul-2008	36.604N	97.486W	0.32
13	Lauder, New Zealand	Feb-2010	45.038S	169.684E	0.37
14	Manaus, Brazil	Jun-2014	3.2133S	60.5986W	0.05
15	Ny Alesund, Spitsbergen	Apr-2002	78.9N	11.9E	0.02
16	Orleans, France	Aug-2009	47.97N	2.113E	0.13
17	Paris, France	Sep-2014	48.486N	2.356E	0.06
18	Park Falls, USA	May-2004	45.945N	90.273W	0.44
19	Reunion Island	Sept-2011	20.901S	55.485E	0.087
20	Rikubetsu, Japan	Nov-2013	43.4567N	143.7661E	0.361
21	Saga, Japan	June-2011	33.240962N	130.288239E	0.007
22	Sodankyla, Finland	Jan-2009	67.3668N	26.6310E	0.188
23	Tsukuba, Japan	Dec-2008	36.0513N	140.1215E	0.03
24	Wollongong, Australia	May-2008	34.406S	150.879E	0.03

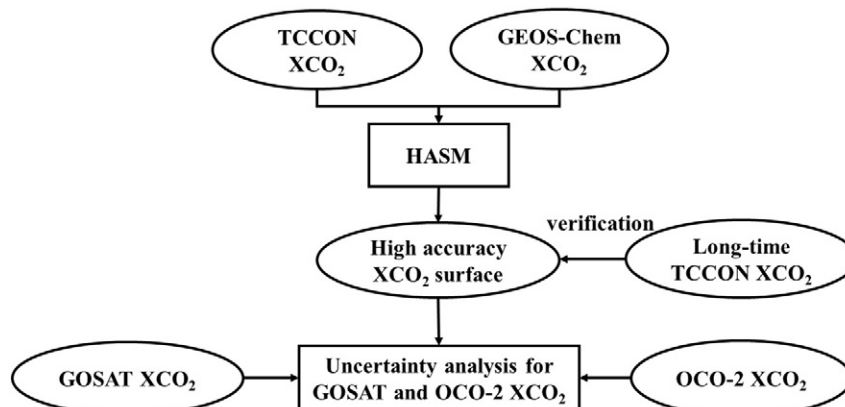


Fig. 2. Flowchart summarizing the procedure used to obtain the high accuracy XCO₂ surface and conduct the evaluation of efficacy of GOSAT and OCO-2 satellite observations.

Table 4
Comparison between monthly HASM XCO₂ predictions and TCCON observations from 1/1/10 to 12/31/15.

TCCON sites	N	ME (ppm)	SD (ppm)	MAE (ppm)
Bialystok	53	−0.15	0.66	0.51
Bremen	60	0.13	1.01	0.82
Darwin	58	−0.35	0.83	0.72
Garmisch	62	0.13	0.73	0.60
Karlsruhe	59	−0.03	0.75	0.58
Lauder	60	0.01	0.50	0.39
Lamont	60	−0.58	0.78	0.75
Orleans	56	0.06	1.05	0.85
Park Falls	60	0.64	0.74	0.82
Wollongong	62	−0.14	0.56	0.45

retrieved from SWIR spectra are released as part of the GOSAT Level 2 product (Yoshida et al., 2011).

For this study, we chose the GOSAT XCO₂ from 9/1/14 to 12/31/14 (V02.31) and 2/1/15 to 8/31/15 (V02.40) to match the OCO-2 and TCCON XCO₂ observations. The data were filtered using the screening procedures described in the data product manual (GOSAT Project, 2013) and the specifications of the data are summarized in Table 1. The largest (26,375) and smallest (6372) number of valid XCO₂ readings were recorded in June and April 2015, respectively. The mean monthly XCO₂ ranged from 394.11 in October 2014 to 398.31 ppm in May 2015 and the standard deviation (Std) of the monthly XCO₂ values varied from 1.96 to 3.09 ppm in most instances.

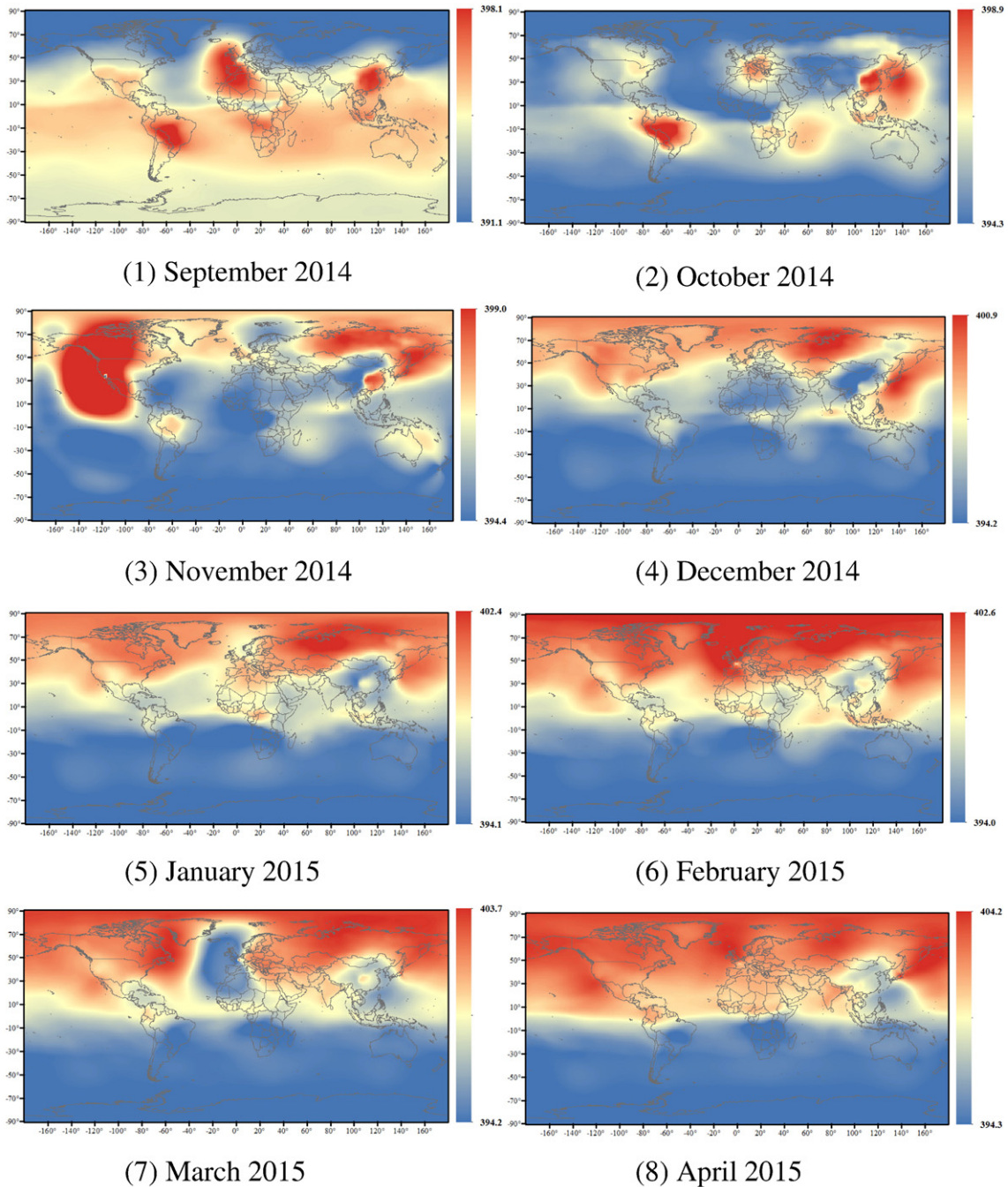


Fig. 3. Monthly HASM XCO₂ surfaces (ppm) at the resolution of 0.5° × 0.5° from September 2014 to August 2015. Each map shows the range of the values in a legend to the right of each map.

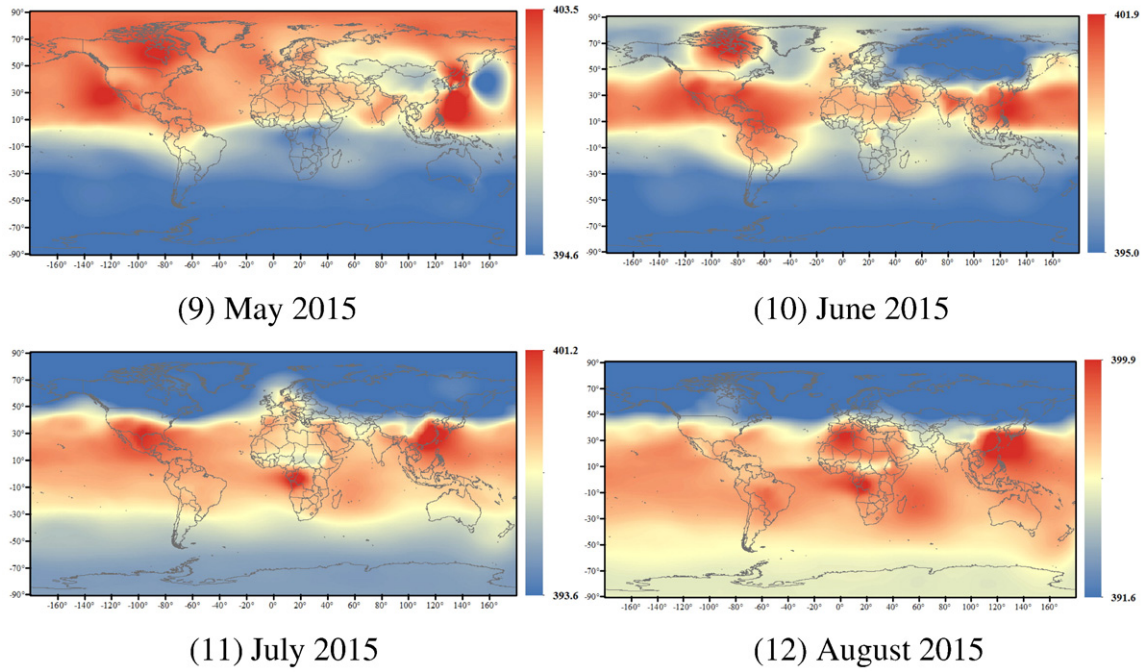


Fig. 3 (continued).

2.2. OCO-2 XCO₂

OCO-2, a copy of OCO-1, was launched in July 2014 and is NASA's first dedicated CO₂ monitoring satellite with high accuracy and resolution on regional scales (Crisp et al., 2017). Unlike GOSAT, OCO-2 carries a single instrument which collects high resolution spectra of reflected solar sunlight in the O₂ A-band (centered near 765 nm) and in the CO₂ bands (centered near 1610 and 2060 nm). The satellite, with a 16 day recurrence, was put in a sun-synchronous orbit at 705 km altitude and the descending node is around 13:36 local time. The instrument creates footprints measuring 1.25 km (width) and 2.4 km (length).

For this study we chose the OCO-2 XCO₂ (OCO2_L2_Lite_FP.7r) observations from 9/1/14 to 8/31/15 and filtered them using the standard criteria described with the product specifications (Mandrake et al., 2013). The metrics for the preprocessed data set are described in Table 2. The largest and smallest number of valid XCO₂ observations over the 12 months were 380,597 and 16,254 in December 2014 and May 2016, respectively. The mean monthly XCO₂ varied from 395.53 ppm in October 2010 to 398.59 ppm in June 2015 and the standard deviation ranged from 0.76 to 1.55 ppm in most instances.

2.3. TCCON XCO₂

The TCCON ground-based network of Fourier transform spectrometers retrieves precise and accurate concentration of CO₂, CH₄, N₂O and CO from near-infrared solar absorption spectra. TCCON provides precise and accurate total column measurements that cannot be matched by satellite remote sensing observations (better than 0.25% for CO₂) (Wunch et al., 2011).

Currently, there are 24 available TCCON sites distributed across the globe (see Fig. 1) whose details can be seen in Table 3. For this study, we conducted a validation experiment based on the TCCON monthly mean XCO₂ observations from 2010 to 2015 to validate the reliability of HASM in modeling the XCO₂ distribution and then modeled the XCO₂ distribution at high accuracy taking the TCCON monthly mean values from 9/1/14 to 8/31/15 as HASM's optimum constrain conditions.

2.4. GEOS-Chem model

GEOS-Chem is a global 3-D chemical transport model for atmospheric composition driven by meteorological data from the Goddard Earth Observing System of the NASA Global Modeling Assimilation Office. This particular model has been widely used by researchers to study the global distribution of atmospheric CO₂ and carbon fluxes (Suntharalingam et al., 2004; Baker et al., 2006).

2.4.1. Inputs and outputs

Driven by meteorological data and emission inventories from fossil fuels, biomass and biofuel burning, ocean exchange, balanced biosphere, and residual annual terrestrial exchange, GEOS-Chem can simulate 3-D spatiotemporal distributions of CO₂ concentrations. The meteorological data have 55 vertical levels, a temporal resolution of 6 h and a horizontal resolution of 1° × 1.25°, which was degraded to 2° × 2.5° for computational efficiency in this study.

The global atmospheric CO₂ monthly mean data were generated for 47 vertical levels using GEOS-Chem (v10-01) with the GEOS-FP meteorological and emission datasets from 2010 to 2015.

2.4.2. XCO₂ estimation

We used a pressure weighting function to obtain GEOS-Chem XCO₂ from the GEOS-Chem CO₂ outputs. The pressure weighting function h relates the local CO₂ concentration specified on discrete pressure levels to the profile-weighted average as follows:

$$XCO_2 = \sum_{i=1}^n h_i u_i \quad (1)$$

$$h_i = \left| \left(-p_i + \frac{p_{i+1} - p_i}{\ln(p_{i+1}/p_i)} \right) + \left(p_i - \frac{p_i - p_{i-1}}{\ln(p_i/p_{i-1})} \right) \right| \frac{1}{p_{surf}} \quad (2)$$

where u denotes the CO₂ concentration, p denotes the pressure, p_{surf} denotes the surface pressure, and the subscripts indicate the layers (Connor et al., 2008; Zhang et al., 2016). This approach applies the left term if $i = 1$ (i.e. $h_1 = |(-p_1 + \frac{p_2 - p_1}{\ln(p_2/p_1)})| \frac{1}{p_{surf}}$, and the right-hand side

term if $i = n$ (i.e. $h_n = |(p_n + \frac{p_n - p_{n-1}}{\ln(p_n/p_{n-1})})|_{p_{surf}}^{-1}$). The approximate XCO₂ was then obtained by averaging the approximate CO₂ concentration at every pressure layer using this pressure weighting function.

2.5. HASM method

2.5.1. Fundamental principles

A surface can be uniquely defined by the first and second fundamental coefficients according to the fundamental theorem of surfaces (Henderson, 1998). The first coefficients describe the intrinsic geometric properties that have little to do with the shape of the surface, which can be achieved from the surface itself (Carmo, 2006). The second fundamental coefficients explain the local warping of the surface, mainly its deviation from a tangent plane at a certain point, which can be studied from outside of the surface (Liseikin, 2004). The Earth's surface system or a component of the Earth's surface environment can be simulated with HASM when its spatial resolution is sufficient (Yue, 2011).

If a surface is a graph of a function $z = f(x, y)$, the first fundamental coefficients E, F and G can be formulated as:

$$\begin{cases} E = 1 + f_x^2 \\ G = 1 + f_y^2 \\ F = f_x \cdot f_y \end{cases} \quad (3)$$

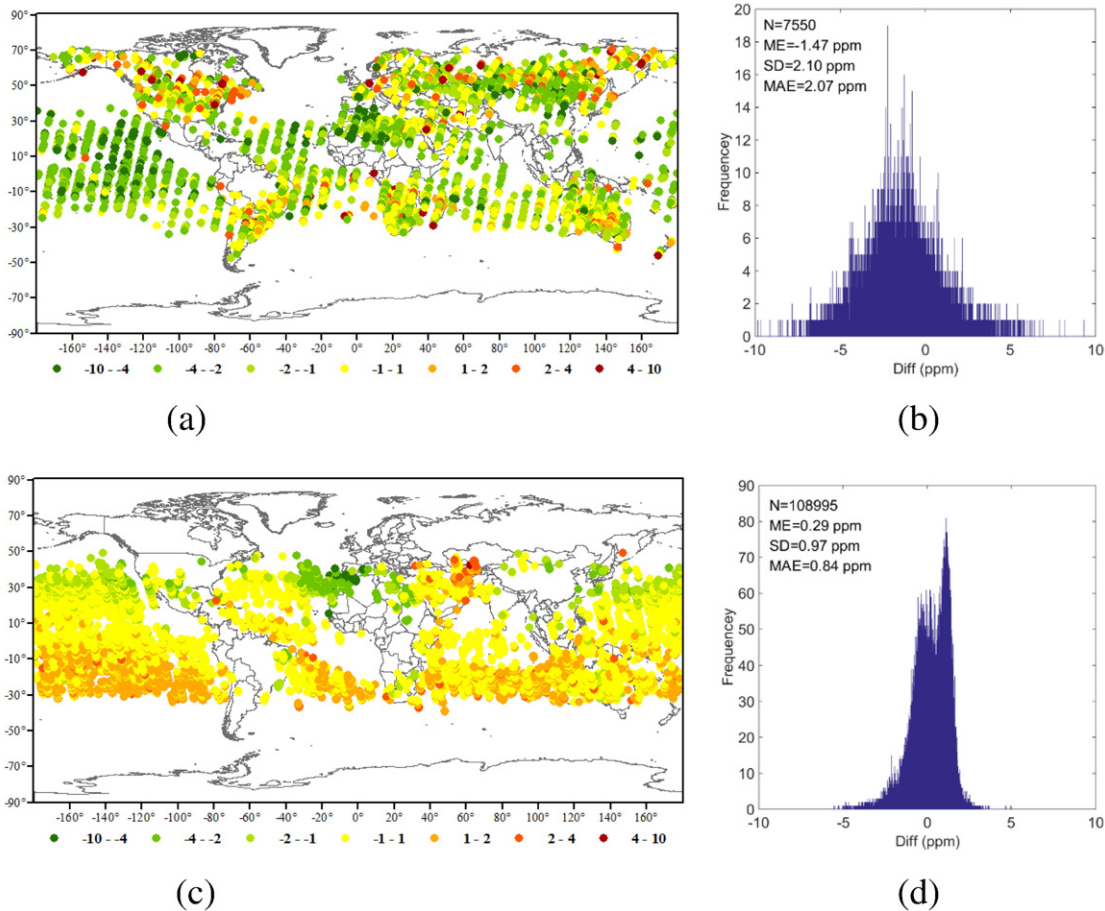
and the second fundamental coefficients L, M and N can be formulated as:

$$\begin{cases} L = \frac{f_{xx}}{\sqrt{1 + f_x^2 + f_y^2}} \\ N = \frac{f_{yy}}{\sqrt{1 + f_x^2 + f_y^2}} \\ M = \frac{f_{xy}}{\sqrt{1 + f_x^2 + f_y^2}} \end{cases} \quad (4)$$

These coefficients should also satisfy the following Gauss equation set:

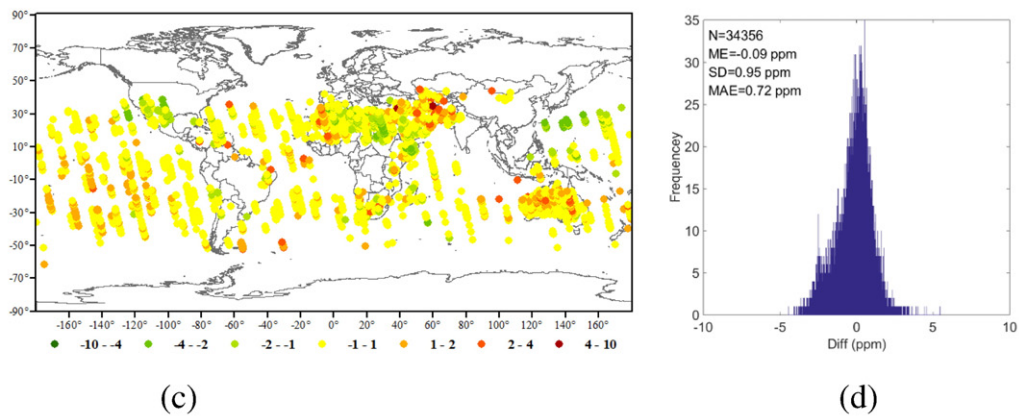
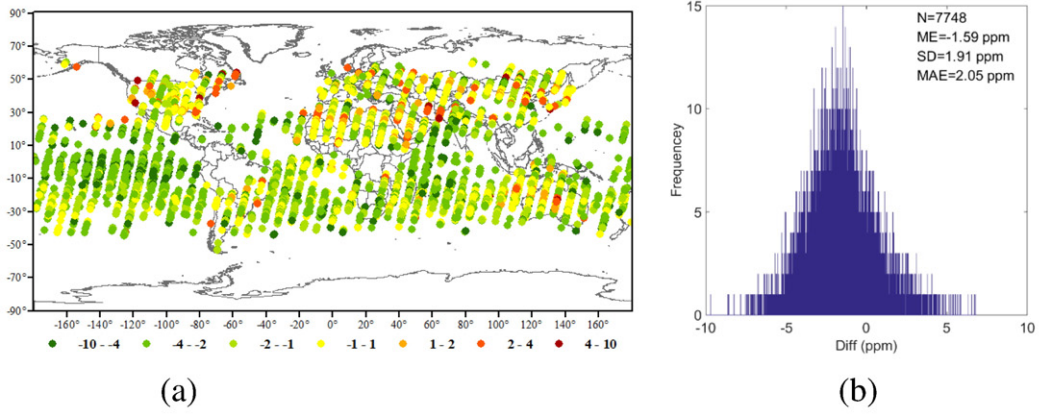
$$\begin{cases} f_{xx} = \Gamma_{11}^1 \cdot f_x + \Gamma_{11}^2 \cdot f_y + L \cdot (E \cdot G - F^2)^{-1/2} \\ f_{yy} = \Gamma_{22}^1 \cdot f_x + \Gamma_{22}^2 \cdot f_y + N \cdot (E \cdot G - F^2)^{-1/2} \\ f_{xy} = \Gamma_{12}^1 \cdot f_x + \Gamma_{12}^2 \cdot f_y + M \cdot (E \cdot G - F^2)^{-1/2} \end{cases} \quad (5)$$

where $\Gamma_{11}^1 = \frac{1}{2}(G \cdot E_x - 2F \cdot F_x + F \cdot E_y) \cdot (E \cdot G - F^2)^{-1}$, $\Gamma_{12}^1 = \frac{1}{2}(G \cdot E_y - F \cdot G_x) \cdot (E \cdot G - F^2)^{-1}$, $\Gamma_{22}^1 = \frac{1}{2}(2G \cdot F_y - G \cdot G_x - F \cdot G_y) \cdot (E \cdot G - F^2)^{-1}$, $\Gamma_{11}^2 = \frac{1}{2}(2E \cdot F_x - E \cdot E_y - F \cdot E_x) \cdot (E \cdot G - F^2)^{-1}$, $\Gamma_{12}^2 = \frac{1}{2}(E \cdot G_x - F \cdot E_y) \cdot (E \cdot G - F^2)^{-1}$, $\Gamma_{22}^2 = \frac{1}{2}(E \cdot G_y - 2F \cdot F_y + F \cdot G_x) \cdot (E \cdot G - F^2)^{-1}$ are the Christoffel symbols of the second kind which depend only on the first fundamental

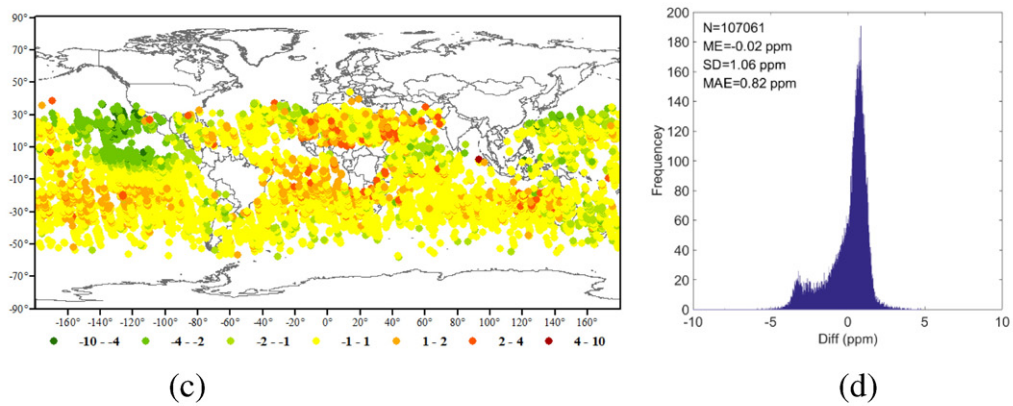
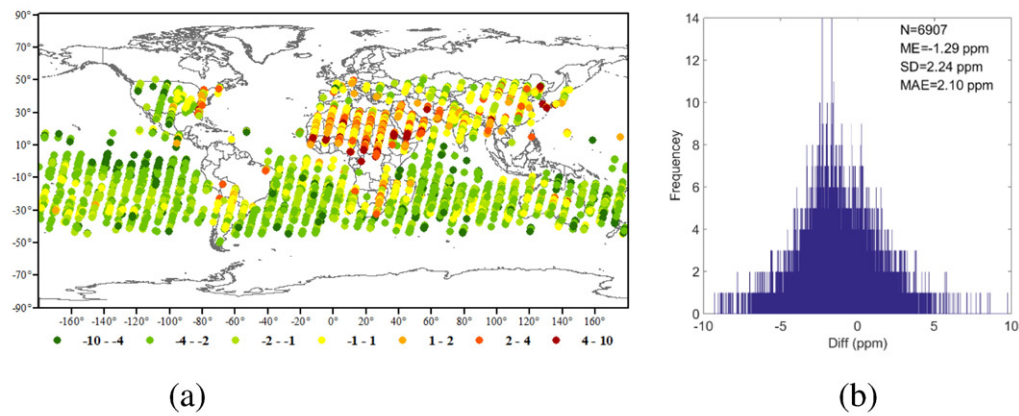


(1) September 2014

Fig. 4. Bias distributions between GOSAT and OCO-2 satellite observations and HASM XCO₂ surfaces (ppm) from September 2014 to August 2015: (a) and (b) Monthly bias distribution for GOSAT and the HASM XCO₂ surface; (c) and (d) Monthly bias distribution for OCO-2 and HASM XCO₂ surface. N records the number of GOSAT/OCO-2 footprints in a certain month, ME is the mean XCO₂ difference, SD is the standard deviation of the difference, and MAE is the mean absolute difference. Colors in maps correspond to values shown in legends below each map.

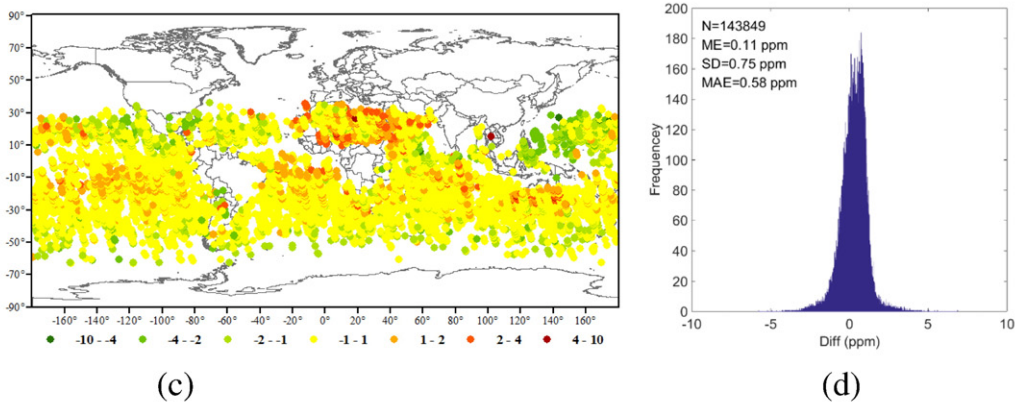
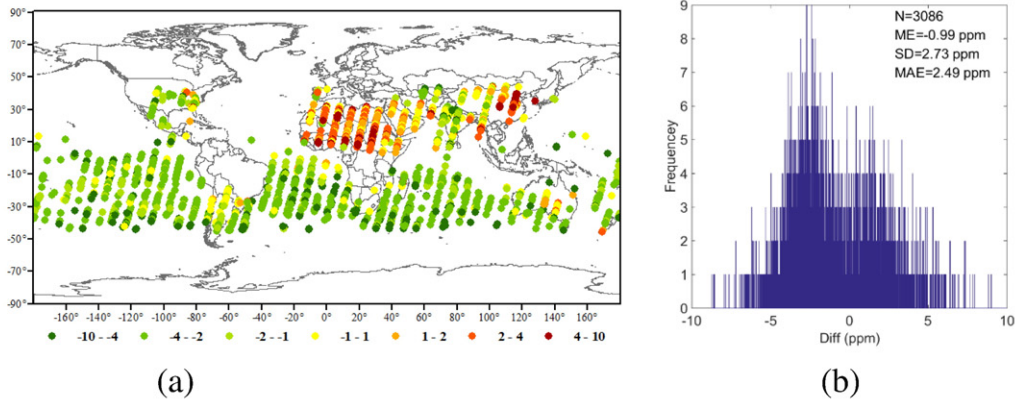


(2) October 2014

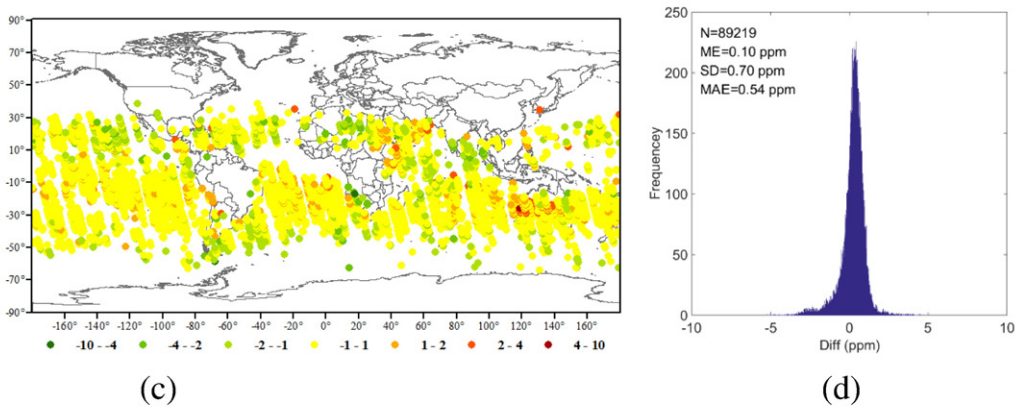


(3) November 2014

Fig. 4 (continued).



(4) December 2014



(5) January 2015

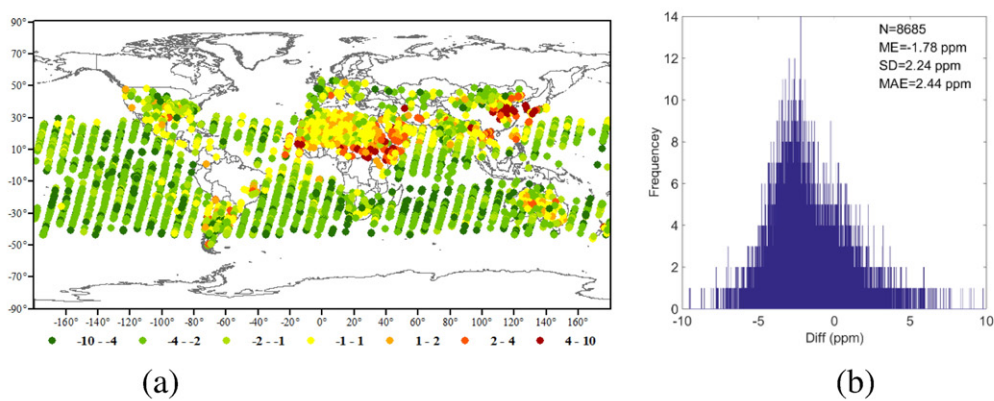
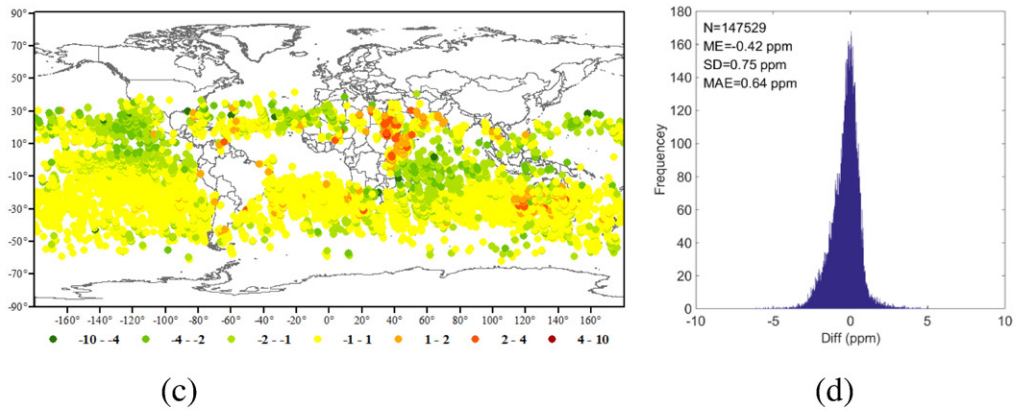
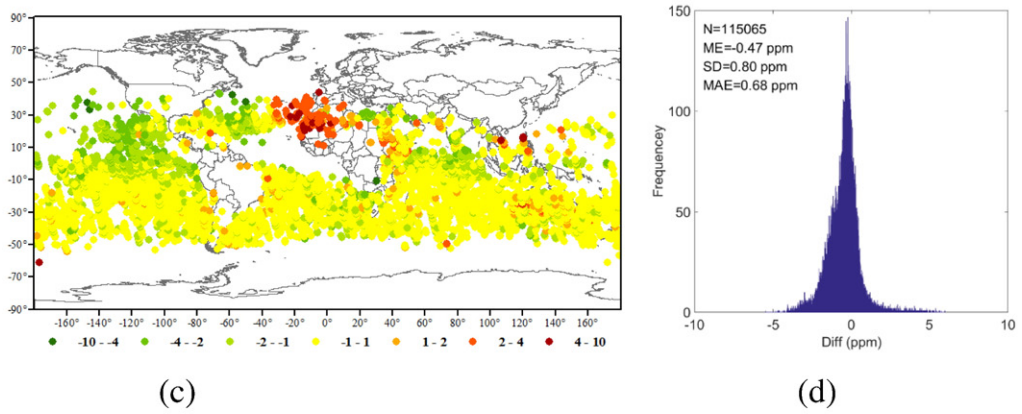
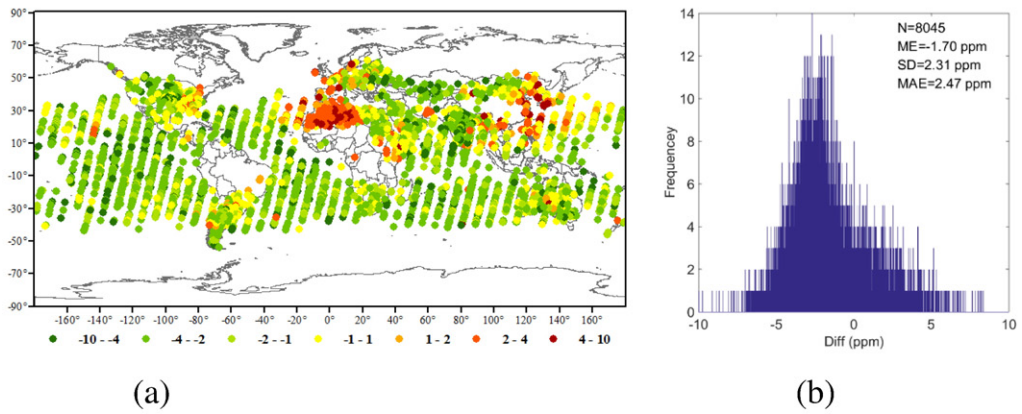


Fig. 4 (continued).



(6) February 2015



(7) March 2015

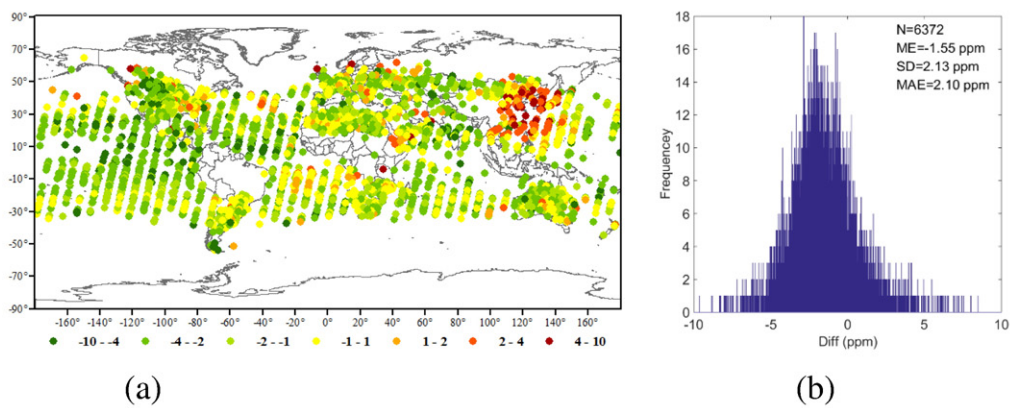
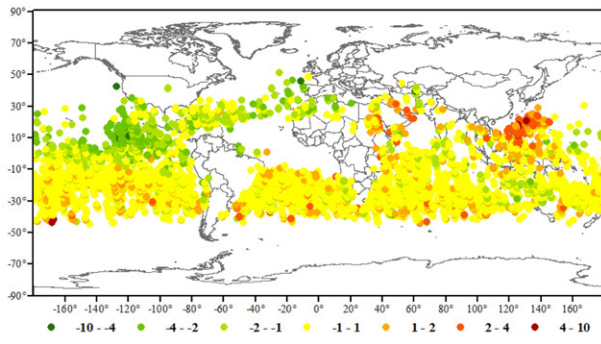
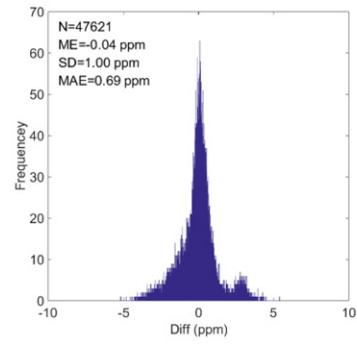


Fig. 4 (continued).

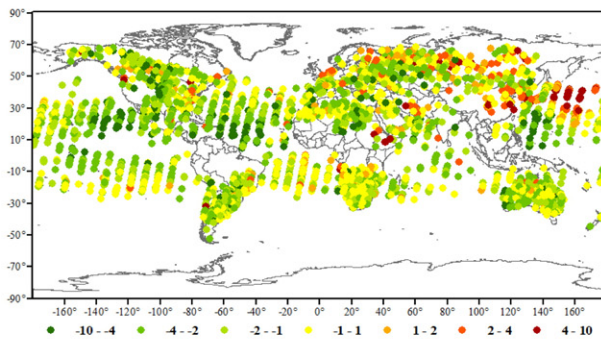


(c)

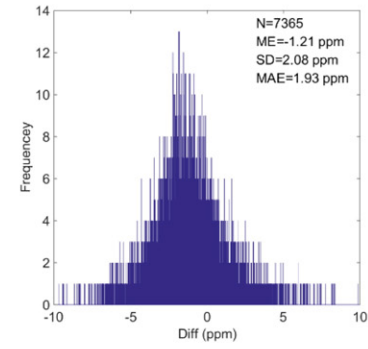


(d)

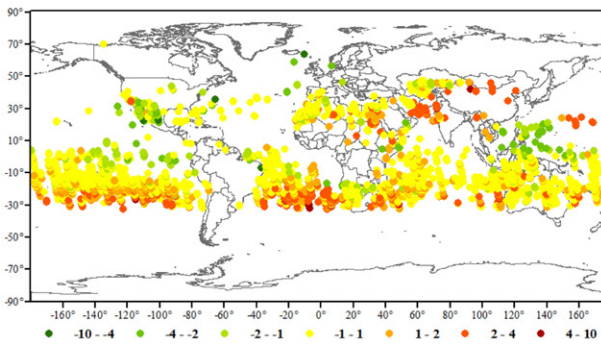
(8) April 2015



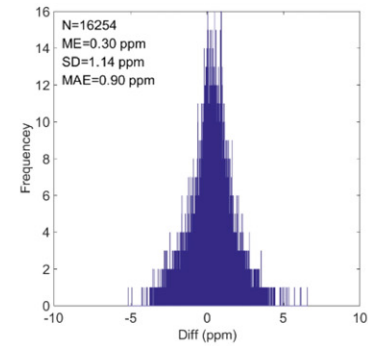
(a)



(b)

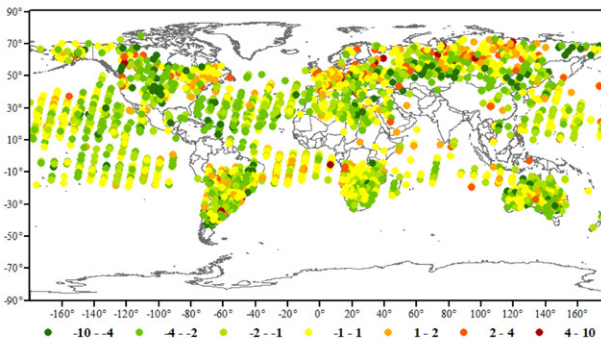


(c)

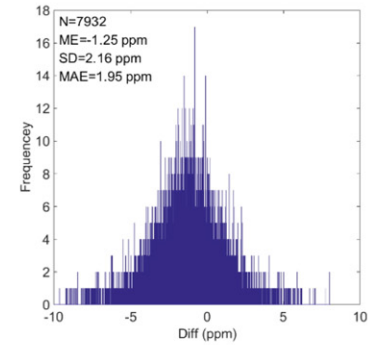


(d)

(9) May 2015



(a)



(b)

Fig. 4 (continued).

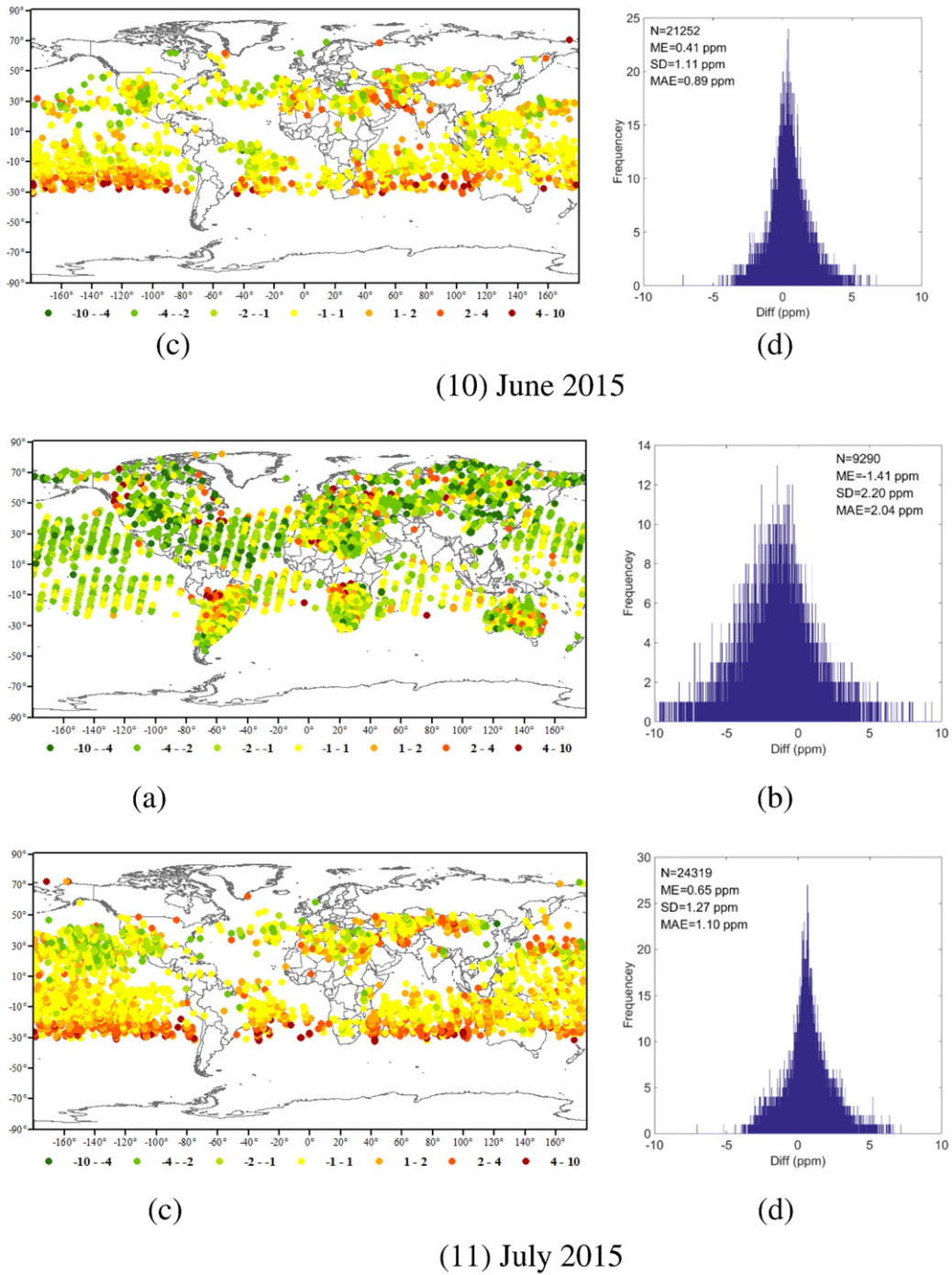


Fig. 4 (continued).

coefficients and their derivatives. Finite difference methods can be used to solve the Gauss equation set (Eq. (5)) and the latter can be simplified with the following equation set (Yue, 2011):

$$\begin{cases} A \cdot z^{(n+1)} = d^{(n)} \\ B \cdot z^{(n+1)} = q^{(n)} \\ C \cdot z^{(n+1)} = p^{(n)} \end{cases} \quad (6)$$

If $f_{i,j}$ is the value of $z = f(x,y)$ at the p th sampled point (x_i, y_i) in the computational domain, the simulation value should be equal or approximately equal to the sampling value of this lattice so that the constraint equation can be added to the simplified equation set (Eq. (6)).

The matrix formulation of the HASM master equations can be expressed as follows:

$$\begin{bmatrix} A \\ B \\ C \\ \lambda \cdot S \end{bmatrix} z^{(n+1)} = \begin{bmatrix} A^T & B^T & C^T & \lambda \cdot S^T \end{bmatrix} \begin{bmatrix} d^{(n)} \\ q^{(n)} \\ p^{(n)} \\ \lambda \cdot k \end{bmatrix} \quad (7)$$

where the parameter λ is the weight of the sampling points and determines the contribution of the sampling points to the simulated surface (Yue, 2011). λ could be a real number, which means all sampling points have the same weight, or λ could be a vector, which means every

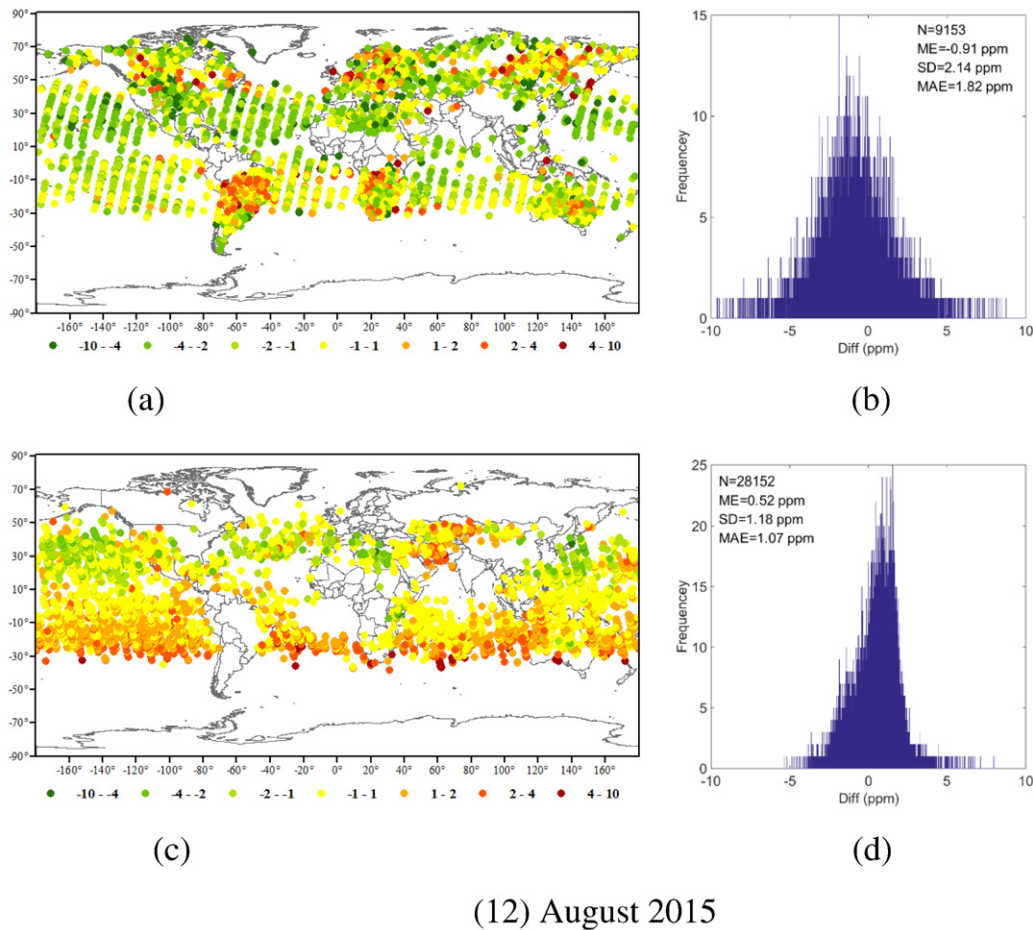


Fig. 4 (continued).

sampling point has its own weight. Smaller values of λ will be selected in complex regions and larger values of λ will be selected in flat regions.

2.5.2. Inputs and outputs

High accuracy surface modeling can simulate constant attribute variations in 3D space, and has been successfully used in model climate change (Wang et al., 2015; Yue et al., 2013a, b), construct DEMs (Yue et al., 2010a, b), interpolate soil properties (Shi et al., 2009, 2016) and terrestrial land cover change (Yue, 2011).

For this study, HASM considered GEOS-Chem XCO₂ as its driving field and TCCON measurements as its optimum control constraints as shown in Eq. (8):

$$X_{sim} = \text{HASM}(X_{initial}, X_{sam}) \quad (8)$$

where X_{sim} is the final XCO₂ surface calculated by HASM, $X_{initial}$ is the approximate XCO₂ surface which is obtained from the GEOS-Chem model, and X_{sam} is the TCCON XCO₂ values. The main inputs of HASM are TCCON XCO₂ and the GEOS-Chem XCO₂ surface with the output being HASM XCO₂.

2.6. Experimental workflow

The TCCON ground-based observations and GOSAT/OCO-2 satellite observations were used with the GEOS-Chem model and HASM interpolation method in the study (Fig. 2). The procedure used to obtain high accuracy XCO₂ surface and evaluate the efficacy of the satellite observations incorporated four steps as follows.

- (1) We obtained monthly GEOS-Chem XCO₂ and TCCON XCO₂ from 1/1/10 to 12/31/15.
- (2) We modeled the XCO₂ surface using HASM, the TCCON observations (as optimum control constraints) and the GEOS-Chem XCO₂ model outputs (as its driving fields) at the TCCON sites with long-term records. We then verified the HASM XCO₂ simulations from 1/1/10 to 12/31/15 by comparing the TCCON observations and HASM XCO₂ predictions.
- (3) We next used HASM to model the XCO₂ surface from 9/1/14 to 8/31/15 taking TCCON observations as its optimum control constraints and the GEOS-Chem atmospheric transport model as its driving field.
- (4) We compared the GOSAT and OCO-2 satellite observations with the HASM XCO₂ surface and the global monthly and annual XCO₂ bias distributions from 9/1/14 to 8/31/15 were employed to depict the uncertainties associated with the satellite estimates of XCO₂.

3. Results

We first describe the HASM-simulated XCO₂ surface and then the monthly and annual XCO₂ bias distributions that were obtained by comparing the global OCO-2 observations with the HASM XCO₂.

3.1. Verification and generation of HASM-simulated XCO₂ surfaces

The HASM method was used to model the XCO₂ surface, taking the GEOS-Chem XCO₂ as its driving field and TCCON measurements as its optimum control constraints to verify the HASM XCO₂ simulations

Table 5
GOSAT and OCO-2 XCO₂ bias distribution by continent from 9/1/14 to 8/31/15.

Continent	GOSAT XCO ₂ bias				OCO-2 XCO ₂ bias			
	N	ME (ppm)	SD (ppm)	MAE (ppm)	N	ME (ppm)	SD (ppm)	MAE (ppm)
Africa	14,928	-0.72	1.97	1.67	59,669	-0.17	1.26	1.00
Asia	12,441	-1.27	2.47	2.20	23,473	0.01	1.50	1.17
Europe	15,625	-1.03	2.74	2.29	252	-0.13	1.46	1.21
North America	6297	-1.49	2.47	2.31	14,137	-0.85	1.10	1.16
Oceania	10,742	-1.20	1.78	1.76	121,649	-0.21	0.84	0.68
South America	3846	-0.72	1.97	1.65	1247	-0.13	1.07	0.85

from 1/1/10 to 12/31/15 and model the HASM XCO₂ surface from 9/1/14 to 8/31/15.

3.1.1. Verification

We chose nine TCCON sites (Table 4) as verification sites, because these sites reported >50 mean monthly XCO₂ values from January 2010 to December 2015. For each verification site, we took the observations from the other sites as HASM's optimum control constraints and GEOS-Chem XCO₂ during the same period as its driving field to simulate the XCO₂ at the verification sites (HASM XCO₂). We then compared the TCCON observations and HASM XCO₂ predictions by comparing the mean error (ME), standard deviation (STD), and mean absolute error (MAE) as follows:

$$ME = \frac{1}{n} \sum_{i=1}^n HASM_i - TCCON_i \tag{9}$$

$$SD = \sqrt{\frac{1}{n} \sum_{i=1}^n (HASM_i - TCCON_i - ME)^2} \tag{10}$$

$$MAE = \frac{1}{n} \sum_{i=1}^n |HASM_i - TCCON_i| \tag{11}$$

From Table 4, we can see that ME and SD for the HASM XCO₂ predictions and TCCON observations are small, with errors mainly within about 1 ppm. The MAEs (0.39–0.85 ppm) show that there are generally no significant differences between TCCON observations and HASM results. These results confirm that the HASM method can simulate XCO₂ with high accuracy.

3.1.2. HASM XCO₂ surface

HASM was next used to model the monthly XCO₂ surface from September 2014 to August 2015 at a resolution of 0.5° × 0.5°, taking GEOS-Chem XCO₂ as its driving field and TCCON measurements as its optimum control constraints. The resulting monthly HASM XCO₂ surfaces are reproduced in Fig. 3 below.

Table 6
GOSAT and OCO-2 annual XCO₂ bias distribution by latitude zone from 9/1/14 to 8/31/15.

latitude (°N)	GOSAT XCO ₂ bias				OCO-2 XCO ₂ bias			
	N	ME (ppm)	SD (ppm)	MAE (ppm)	N	ME (ppm)	SD (ppm)	MAE (ppm)
35°–45°	6547	-1.24	2.52	2.22	16,561	-0.40	1.51	1.31
25°–35°	10,542	-0.85	2.12	1.82	55,295	-0.48	1.24	1.06
15°–25°	10,371	-1.23	2.05	2.03	81,672	-0.35	1.16	0.93
5°–15°	3617	-1.13	2.77	2.51	30,105	-0.41	1.23	0.97
-5°–5°	3888	-2.35	1.91	2.63	71,548	-0.53	0.97	0.88
-15° to -5°	8379	-1.41	2.03	2.05	85,674	0.09	0.78	0.64
-25° to -15°	14,336	-1.48	1.68	1.86	232,130	0.28	0.84	0.69
-35° to -25°	9770	-1.63	1.80	2.02	241,785	0.10	0.76	0.58
-45° to -35°	2646	-2.60	1.78	2.74	57,199	-0.10	0.53	0.41

The 12 maps reproduced in Fig. 3 show how the XCO₂ distribution varies by month. The 12 maps display three general trends. First, the XCO₂ in the equatorial regions is higher than that in other regions in October 2014 and June and July 2015. Second, the highest and lowest XCO₂ occur in equatorial regions and the northern hemisphere, respectively in September 2014 and August 2015. Third, the XCO₂ in the northern hemisphere is higher than that in the southern hemisphere from November 2014 to May 2015, which can be attributed to the reductions in the absorbing ability of vegetation and/or increased anthropogenic emissions in the northern hemisphere winter.

Simultaneously, a number of monthly XCO₂ anomalies can be seen. For example, in September 2014, there are higher XCO₂ in some regions, such as in Brazil, northwest Africa, the Iberian Peninsula, the UK, and East Asia. In October 2014, the XCO₂ in the northern half of South America, East Asia, eastern Europe is obviously higher than in other regions. In March 2015, the XCO₂ over the northern Atlantic Ocean and western Europe is obviously lower than in the other months.

3.2. GOSAT and OCO-2 observations compared to HASM XCO₂ surface

We next compared the GOSAT and OCO-2 satellite observations with the HASM XCO₂ surface by analyzing the global monthly and annual XCO₂ bias distribution from 9/1/14 to 8/31/15.

3.2.1. Global monthly XCO₂ bias distribution

From Fig. 4(a, c), we can see that most satellite observations cover the middle and lower latitudes and the XCO₂ bias in the lower latitudes is generally lower than that in the middle latitudes. In addition, the differences between GOSAT and the HASM XCO₂ surface range from -10 to 10 ppm with a mode of -4 to -2 ppm, while the differences between OCO-2 and the HASM XCO₂ surface range from -5 to 5 ppm with a mode of -1 to 1 ppm.

Fig. 4(b, d) show that the distribution of the differences between the satellite observations and the HASM XCO₂ surface are consistent with a normal distribution, with the differences between OCO-2 and the HASM XCO₂ surface mimicking a standard normal distribution. The mean annual bias of GOSAT is -1.38 ppm and the GOSAT XCO₂ values are lower than the corresponding HASM XCO₂ values in every month. However, the mean annual bias of OCO-2 XCO₂ is 0.2 ppm, and OCO-2 XCO₂ values are higher than the HASM XCO₂ values in all months except March and April 2015. The MAEs of the GOSAT XCO₂ bias range from 1.82 ppm in August 2015 to 2.49 ppm in December 2014 while the MAEs of the OCO-2 XCO₂ bias range from 0.54 ppm in January 2015 to 1.10 ppm in July 2015. In addition, the smallest MAE of GOSAT XCO₂ bias is still larger than the largest MAE of OCO-2 XCO₂ bias during the 12 month period September 2014 to August 2015.

Overall, the OCO-2 and GOSAT XCO₂ observations agree reasonably well with the HASM XCO₂ surface, but the OCO-2 XCO₂ observations show better agreement with the HASM XCO₂ surface than the GOSAT XCO₂ observations.

3.2.2. Global annual XCO₂ bias distribution

We also calculated the global annual XCO₂ bias distribution for GOSAT and OCO-2 and compared the bias distribution by continent, latitude and longitude zone.

3.2.2.1. XCO₂ bias distribution by continent. The satellite bias distribution varied when we compared the GOSAT and OCO-2 annual XCO₂ bias in Africa, Asia, Europe, North America, Oceania and South America.

From Table 5, we can see that the GOSAT XCO₂ bias is larger than the OCO-2 bias. The MAE of the GOSAT annual XCO₂ bias, for example, ranged from 1.65 ppm in South America to 2.31 ppm in North America, whereas the MAE of the OCO-2 annual XCO₂ bias ranged from 0.68 ppm in Oceania to 1.21 ppm in Europe. In addition, the GOSAT XCO₂ bias exceeded the OCO-2 XCO₂ bias in every continent and was more than twice as much in the case of Oceania.

Taken as a whole, the OCO-2 annual XCO₂ observations agreed better with the HASM annual XCO₂ surface for every continent.

3.2.2.2. XCO₂ bias distribution by latitude zone. We next divided the observations into nine classes, one for every 10° of latitude between 45°S and 45°N, and compared the GOSAT and OCO-2 XCO₂ bias distribution by latitude zone.

From Table 6, we can see that the smallest MAEs for the GOSAT XCO₂ bias are 1.82 ppm (25–35°N) and 1.86 ppm (15–25°S), while the largest MAEs are 2.74 ppm (35–45°S), 2.63 ppm (5°S–5°N) and 2.51 ppm (5–15°N).

From Table 6, we can also see that the smallest MAE for the OCO-2 XCO₂ bias is 0.41 ppm between 35° and 45°S while the largest MAE is 1.31 ppm between 35° and 45°N. Moreover, the MAE gradually increases from south to north.

Overall, the OCO-2 observations produced a better fit with the HASM XCO₂ surface than the GOSAT observations, especially in the southern hemisphere.

3.2.2.3. XCO₂ bias distribution by longitude zone. We next divided the observations into nine classes, one for every 40° of longitude, and compared the GOSAT and OCO-2 XCO₂ bias distribution by longitude zone.

From Table 7, we can see that the smallest MAEs of the GOSAT XCO₂ bias are 1.81 ppm (20°W–20°E) and 1.86 ppm (20–60°E), and the largest MAE is 2.66 ppm (100–140°W).

From Table 7, we can also see that the OCO-2 XCO₂ bias is smaller than the GOSAT XCO₂ bias (as would be expected given the results presented previously). The smallest MAE of the OCO-2 XCO₂ bias is 0.55 ppm between 60 and 100°W and the largest MAE is 0.84 ppm between 100 and 140°W. The variations in the MAEs show no obvious change with longitude.

4. Discussion and conclusions

Ground observations are able to capture CO₂ concentrations accurately and can be used to evaluate satellite observation data. However, the number of TCCON sites is too small to conduct a comprehensive

analysis of the efficacy of satellite datasets. Similarly, atmospheric transport models can provide continuous atmospheric CO₂ concentrations in space and time, but the accuracy of the model outputs need to be verified, especially for regions with large emissions. HASM can model a continuous XCO₂ surface with high accuracy taking TCCON observations as its optimum control constraints and an atmospheric transport model outputs as its driving field. The MAE of bias ranged from 0.39 to 0.85 ppm with the lowest values occurring at the Lauder site in New Zealand (0.39 ppm) and Wollongong site in Australia (0.45 ppm). These results show that the smaller land mass and populations in the southern hemisphere provides better model performance as well as lower XCO₂ values overall. The results also indicate that HASM did reasonably well in modeling global atmospheric XCO₂ in the northern hemisphere where numerous studies have shown how human activities, such as fossil fuel combustion, cement production and deforestation, can lead to higher regional CO₂ concentrations in the atmosphere (Kong et al., 2011; Le Quéré et al., 2015; Eldering et al., 2017).

Given these results, we felt justified in using the HASM XCO₂ surface to evaluate the efficacy of the GOSAT and OCO-2 XCO₂ observations. We first modeled the HASM XCO₂ surface by fusing the TCCON measurements and the GEOS-Chem XCO₂ model outputs for the period 9/1/14 to 8/31/15 and the used the bias distribution statistics to compare the GOSAT and OCO-2 satellite observations with the HASM XCO₂ surface. The results showed that the OCO-2 XCO₂ observations agree much better with the HASM XCO₂ surface than the GOSAT XCO₂ observations do for both the monthly and annual time intervals. The explanation is a function of the volume of data given that OCO-2 returns almost 1 million soundings over the sunlit hemisphere each day and on monthly timescales, between 7 and 12% of these soundings pass the cloud screens and other data quality filters to yield full-column estimates of XCO₂ (Crisp et al., 2017). However, GOSAT measures several tens of thousands of single soundings in three days, and only about 10% of these satellite soundings are available for gas retrievals under clear-sky conditions (Oshchepkov et al., 2012). Therefore, OCO-2 produces more data than GOSAT and the results of this study indicate that this matters. The comparison with the HASM XCO₂ surface shows that OCO-2 is likely to provide more reliable estimates of the global patterns of XCO₂ than GOSAT.

However, the results also showed how the efficacy of the OCO-2 and GOSAT estimates varied geographically. These variations may depend on the sensor performance and retrieval algorithms used in addition to the volume of data produced. The OCO-2 retrieval algorithm is similar to the GOSAT retrieval algorithm (O'Dell et al., 2012; Crisp et al., 2012; Eldering et al., 2017). This evident from those parts of atmosphere that displayed large MAEs. From Table 6, for example, the MAE of XCO₂ bias between 35°S and 40°S is obviously larger than for other latitude zones for both OCO-2 and GOSAT. The same is true for high MAEs reported between 100°W and 140°W (Table 7) and the common feature of both of these zones is that surface is ocean. The OCO-2 observations may show less bias in these instances because of the larger number of observations and because the OCO-2 mission team has modified their data acquisition strategy to accommodate over still water with a layer

Table 7
GOSAT and OCO-2 annual XCO₂ bias distribution by longitude zone from 9/1/14 to 8/31/15.

Longitude (°E)	GOSAT XCO ₂ bias				OCO-2 XCO ₂ bias			
	N	ME (ppm)	SD (ppm)	MAE (ppm)	N	ME (ppm)	SD (ppm)	MAE (ppm)
140°–180°	9437	–1.31	2.20	2.05	126,100	–0.04	0.82	0.63
100°–140°	20,134	–1.07	2.30	2.00	217,725	–0.05	0.94	0.71
60°–100°	13,028	–1.74	2.21	2.30	119,062	0.05	0.99	0.73
20°–60°	27,847	–0.93	2.13	1.86	165,742	–0.21	1.10	0.84
–20°–20°	18,834	–0.79	2.17	1.81	170,306	0.12	0.89	0.68
–60° to –20°	12,057	–1.52	2.01	2.06	71,568	–0.02	0.83	0.60
–100° to –60°	13,205	–1.70	2.08	2.22	90,839	0.04	0.74	0.55
–140° to –100°	15,218	–2.38	1.96	2.66	245,303	–0.18	1.10	0.84
–180° to –140°	7900	–2.19	1.60	2.32	171,693	0.10	0.85	0.66

of highly reflective material on its surface that would otherwise lead to elevated measurements (Eldering et al., 2017).

Quantitative evaluations of satellites observation like that conducted here are important and will improve the investigation of carbon sources and sinks and our understanding of global carbon cycling. The results from this study showed: (1) both the OCO-2 and GOSAT satellite observations document how elevated XCO₂ concentrations frequently occur over large populated areas in the northern hemisphere; and (2) that the OCO-2 satellite observations offer more reliable estimates of XCO₂ than the GOSAT satellite observations, while noting some potential problems with the performance of both satellites over ocean surfaces.

The overall results were encouraging and this study should be repeated as more satellite data for measuring CO₂ becomes available due to larger numbers of satellites and/or longer time series for the existing carbon satellites. The HASM approach used for this study can be expected to provide better precision so long as the number of ground observation sites increases over time as well.

Acknowledgments

This work was supported by the National Natural Science Foundation of China (Grant Nos. 91325204, 41421001 and 41590844) and a Land Resources and Environmental Information System (LREIS) Innovation Project (Grant No. O88RA600YA). We are grateful for the data products provided by the NIES GOSAT, OCO-2 and TCCON Projects. We also thank the GEOS-Chem team for providing access to GEOS-Chem for this work.

References

- Baker, D.F., Law, R.M., Gurney, K.R., Rayner, P., Peylin, P., Denning, A.S., Bousquet, P., Bruhwiler, L., Chen, Y.H., Ciais, P., Fung, I.Y., Heimann, M., John, J., Maki, T., Maksyutov, S., Masarie, K., Prather, M., Pak, B., Taguchi, S., Zhu, Z., 2006. TransCom 3 inversion intercomparison: impact of transport model errors on the interannual variability of regional CO₂ fluxes, 1988–2003. *Glob. Biogeochem. Cycles* 20, 313–324.
- Barkley, M.P., Monks, P.S., Frie, U., Mittermeier, R.L., 2006. Comparisons between SCIAMACHY atmospheric CO₂ retrieved using (FSI) WFM-DOAS to ground based FTIR data and the TM3 chemistry transport model. *Atmos. Chem. Phys.* 6, 4483–4498.
- Belikov, D.A., Bril, A., Maksyutov, S., Oshchepkov, S., Saeki, T., Takagi, H., Yoshida, Y., Ganshin, A., Zhuravlev, R., Aoki, S., Yokota, T., 2014. Column-averaged CO₂ concentrations in the subarctic from GOSAT retrievals and NIES transport model simulations. *Polar Sci.* 8 (2), 1–17.
- Bey, I., Jacob, D.J., Yantosca, R.M., Logan, J.A., Field, B.D., Fiore, A.M., Li, Q., Liu, H.Y., Mickley, L.J., Schultz, M.G., 2001. Global modeling of tropospheric chemistry with assimilated meteorology: model description and evaluation. *J. Geophys. Res.* 106, 23073–23095.
- Boesch, H., Baker, D., Connor, B., Crisp, D., Miller, C., 2011. Global characterization of CO₂ column retrievals from shortwave-infrared satellite observations of the orbiting carbon observatory-2 mission. *Remote Sens.* 3, 270–304.
- Bosch, H., Toon, G.C., Sen, B., Washenfelder, R.A., Wennberg, P.O., Buchwitz, M., Beek, R., Burrows, J.P., Crisp, D., Christi, M., Connor, B.J., Natraj, V., Yung, Y.L., 2006. Space-based near-infrared CO₂ measurements: testing the orbiting carbon observatory retrieval algorithm and validation concept using SCIAMACHY observations over Park Falls, Wisconsin. *J. Geophys. Res.* 111, D23302.
- Bovensmann, H., Burrows, J.P., Buchwitz, M., Frerick, J., Noél, S., Rozanov, V., Chance, K.V., Goede, A., 1999. SCIAMACHY—mission objectives and measurement modes. *J. Atmos. Sci.* 56, 127–150.
- Burrows, J.P., Hölzle, E., Goede, A.P.H., Visser, H., Fricke, W., 1995. SCIAMACHY—scanning imaging absorption spectrometer for atmospheric cartography. *Acta Astronaut.* 35, 445–451.
- Carmo, M.P., 2006. *Differential Geometry of Curves and Surfaces*. China Machine Press, Beijing, China.
- Chevallier, F., Bréon, F.M., Rayner, P.J., 2007. Contribution of the orbiting carbon observatory to the estimation of CO₂ sources and sinks: theoretical study in a variational data assimilation framework. *J. Geophys. Res.* 112, D09307.
- Chevallier, F., Maksyutov, S., Bousquet, P., Bréon, F.M., Saito, R., Yoshida, Y., Yokota, T., 2009. On the accuracy of the CO₂ surface fluxes to be estimated from the GOSAT observations. *Geophys. Res. Lett.* 36, L19807.
- Connor, B.J., Boesch, H., Toon, G., Sen, B., Miller, C., Crisp, D., 2008. Orbiting carbon observatory: inverse method and prospective error analysis. *J. Geophys. Res.* 113, D05305.
- Crisp, D., Atlas, R.M., Bréon, F.M., Brown, L.R., Burrows, J.P., Ciais, P., Connor, B.J., Doney, S.C., Fung, I.Y., Jacob, D.J., Miller, C.E., O'Brien, D., Pawson, S., Randerson, J.T., Rayner, P., Salawitch, R.S., Sander, S.P., Sen, B., Stephens, G.L., Tans, P.P., Toon, G.C., Wennberg, P.O., Wofsy, S.C., Yung, Y.L., Kuang, Z., Chudasama, B., Sprague, G., Weiss, P., Pollock, R., Kenyon, D., Schroll, S., 2004. The orbiting carbon observatory (OCO) mission. *Adv. Space Res.* 34, 700–709.
- Crisp, D., Fisher, B.M., O'Dell, C., Frankenberg, C., Basilio, R., Bösch, H., Brown, L.R., Castano, R., Connor, B., Deutscher, N.M., Eldering, A., Griffith, D., Gunson, M., Kuze, A., Mandrake, L., McDuffie, J., Messerschmidt, J., Miller, C.E., Morino, I., Natraj, V., Notholt, J., O'Brien, D.M., Oyafuso, F., Polonsky, I., Robinson, J., Salawitch, R., Sherlock, V., Smyth, M., Suto, H., Taylor, T.E., Thompson, D.R., Wennberg, P.O., Wunch, D., Yung, Y.L., 2012. The ACOS CO₂ retrieval algorithm – part II: global XCO₂ data characterization. *Atmos. Meas. Tech.* 5, 687–707.
- Crisp, D., Pollock, H.R., Rosenberg, R., Chapsky, L., Lee, R.A.M., Oyafuso, F.A., Frankenberg, C., O'Dell, C.W., Bruegge, C.J., Doran, G.B., Eldering, A., Fisher, B.M., Fu, D., Gunson, M.R., Mandrake, L., Osterman, G.B., Schwandner, F.M., Sun, K., Taylor, T.E., Wennberg, P.O., Wunch, D., 2017. The on-orbit performance of the orbiting carbon observatory-2(OCO-2) instrument and its radiometrically calibrated products. *Atmos. Meas. Tech.* 10, 59–81.
- Eldering, A., O'Dell, C.W., Wennberg, P.O., Crisp, D., Gunson, M.R., Viatte, C., Avis, C., Braverman, A., Castano, R., Chang, A., Chapsky, L., Cheng, C., Connor, B., Dang, L., Doran, G., Fisher, B., Frankenberg, C., Fu, D., Granat, R., Hobbs, J., Lee, R.A.M., Mandrake, L., Duffie, J.M., Miller, C.E., Myers, V., Natraj, V., O'Brien, D., Osterman, G.B., Oyafuso, F., Payne, V.H., Pollock, H.R., Polonsky, I., Roehl, C.M., Rosenberg, J., Schwandner, F., Smyth, M., Tang, V., Taylor, T.E., To, C., Wunch, D., Yoshimizu, Z., 2017. The orbiting carbon observatory-2: first 18 months of science data products. *Atmos. Meas. Tech.* 10, 549–563.
- Feng, L., Palmer, P.I., Yang, Y., Yantosca, R.M., Kawa, S.R., Paris, J.D., Matsueda, H., Machida, T., 2011. Evaluating a 3-D transport model of atmospheric CO₂ using ground-based, aircraft, and space-borne data. *Atmos. Chem. Phys.* 11, 2789–2803.
- GOSAT Project, 2013. NIES GOSAT TANSO-FTS WSIR Level 2 Data Product Format Description.
- Henderson, D.W., 1998. *Differential Geometry*. Prentice-Hall, London, UK.
- IPCC (Intergovernmental Panel on Climate Change), 2014. *Climate Change Synthesis Report. Contribution of Working Groups I, II and III to the Fifth Assessment Report of the IPCC*. Geneva, Switzerland.
- Kong, S.F., Lu, B., Han, B., Bai, Z.P., Xu, Z., You, Y., Jin, L.M., Guo, X.Y., Wang, R., 2011. Seasonal variation analysis of atmospheric CH₄, N₂O and CO₂ in Tianjin off shore area. *Sci. China Earth Sci.* 53, 1205–1215.
- Kuze, A., Suto, H., Nakajima, M., Hamazaki, T., 2009. Thermal and near infrared sensor for carbon observation Fourier-transform spectrometer on the greenhouse gases observing satellite for greenhouse gases monitoring. *Appl. Opt.* 48, 6716–6733.
- Le Quéré, C., Moriarty, R., Andrew, R.M., Canadell, J.G., Sitch, S., Korsbakken, J.I., Friedlingstein, P., Peters, G.P., Andres, R.J., Boden, T.A., Houghton, R.A., House, J.I., Keeling, R.F., Tans, P., Arneeth, A., Bakker, D.C.E., Barbero, L., Bopp, L., Chang, J., Chevallier, F., Chini, L.P., Ciais, P., Fader, M., Feely, R.A., Gkritzalis, T., Harris, I., Hauck, J., Ilyina, T., Jain, A.K., Kato, E., Kitidis, V., Klein Goldewijk, K., Koven, C., Landschützer, P., Lauvset, S.K., Lefèvre, N., Lenton, A., Lima, I.D., Metzl, N., Millero, F., Munro, D.R., Murata, A., Nabel, J.E.M.S., Nakaoka, S., Nojiri, Y., O'Brien, K., Olsen, A., Ono, T., Pérez, F.F., Pfeil, B., Pierrot, D., Poulter, B., Rehder, G., Rödenbeck, C., Saito, S., Schuster, U., Schwinger, J., Séférian, R., Steinhoff, T., Stocker, B.D., Sutton, A.J., Takahashi, T., Tilbrook, B., van der Laan-Luijckx, I.T., van der Werf, G.R., van Heuven, S., Vandemark, D., Viovy, N., Wiltshire, A., Zaehle, S., Zeng, N., 2015. Global carbon budget 2015. *Earth Syst. Sci. Data* 7, 349–396.
- Lei, L.P., Guan, X.H., Zeng, Z.C., Zhang, B., Ru, F., Bu, R., 2014. A comparison of atmospheric CO₂ concentration GOSAT-based observations and model simulations. *Sci. China Earth Sci.* 57, 1393–1402.
- Liseikin, V.D., 2004. *A Computational Differential Geometry Approach to Grid Generation*. Springer, Berlin, Germany.
- Liu, Y., Yang, D.X., 2016. Advancements in theory of GHG observation from space. *Chin. Sci. Bull.* 61 (5), 349–352.
- Liu, Y., Cai, Z.N., Yang, D.X., Zheng, Y.Q., Duan, M.Z., Lv, D.R., 2014. Effects of spectral sampling rate and range of CO₂ absorption bands on XCO₂ retrieval from tan sat hyperspectral spectrometer. *Chin. Sci. Bull.* 59 (14), 1485–1491.
- Mandrake, L., Frankenberg, C., O'Dell, C.W., Osterman, G., Wennberg, P., Wunch, D., 2013. Semi-autonomous sounding selection for OCO-2. *Atmos. Meas. Tech.* 6, 2851–2864.
- O'Dell, C.W., Connor, B., Bösch, H., O'Brien, D., Frankenberg, C., Castano, R., Christi, M., Eldering, D., Fisher, B., Gunson, M., McDuffie, J., Miller, C.E., Natraj, V., Oyafuso, F., Polonsky, I., Smyth, M., Taylor, T., Toon, G.C., Wennberg, P.O., Wunch, D., 2012. The ACOS CO₂ retrieval algorithm – part 1: description and validation against synthetic observations. *Atmos. Meas. Tech.* 5, 99–121.
- Oshchepkov, S., Bril, A., Yokota, T., Morino, I., Yoshida, Y., Matsunaga, T., Belikov, D., Wunch, D., Wennberg, P., Toon, G., O'Dell, C., Butz, A., Guerlet, S., Cogan, A., Boesch, H., Eguchi, N., Deutscher, N., Griffith, D., Macatangay, R., Notholt, J., Sussmann, R., Rettinger, M., Sherlock, V., Robinson, J., Kyrö, E., Heikkinen, P., Feist, D.G., Nagahama, T., Kadygrov, N., Maksyutov, S., Uchino, O., Watanabe, H., 2012. Effects of atmospheric light scattering on spectroscopic observations of greenhouse gases from space: validation of PPDF-based CO₂ retrievals from GOSAT. *J. Geophys. Res.* 117, D12305.
- Rayner, P.J., O'Brien, D.M., 2001. The utility of remotely sensed CO₂ concentration data in surface source inversions. *Geophys. Res. Lett.* 28, 175–178.
- Reuter, M., Bovensmann, H., Buchwitz, M., Burrows, J.P., Connor, B.J., Deutscher, N.M., Griffith, D.W.T., Heymann, J., Keppel-Aleks, G., Messerschmidt, J., Notholt, J., Petri, C., Robinson, J., Schneising, O., Sherlock, V., Velasco, V., Warneke, T., Wennberg, P.O., Wunch, D., 2011. Retrieval of atmospheric CO₂ with enhanced accuracy and precision from SCIAMACHY: validation with FTS measurements and comparison with model results. *J. Geophys. Res.* 116, D04301.
- Shi, W.J., Liu, J.Y., Song, Y.J., Du, Z.P., Chen, C.F., Yue, T.X., 2009. Surface modelling of soil pH. *Geoderma* 150, 113–119.
- Shi, W.J., Yue, T.X., Du, Z.P., Wang, Z., Li, X.W., 2016. Surface modeling of soil antibiotics. *Sci. Total Environ.* 543, 609–619.
- Shim, C., Nassar, R., Kim, J., 2011. Comparison of model-simulated atmospheric carbon dioxide with GOSAT retrievals. *Asian J. Atmos. Environ.* 5, 263–277.
- Suntharalingam, P., Jacob, D.J., Palmer, P.I., Logan, J.A., Yantosca, R.M., Xiao, Y., Evans, M.J.M., 2004. Improved quantification of Chinese carbon fluxes using CO₂/CO correlations in Asian out-flow. *J. Geophys. Res.* 109, D18S18.

- Wang, C.L., Zhao, N., Yue, T.X., Zhao, M.W., Chen, C., 2015. Change trend of monthly precipitation in China with an improved surface modeling method. *Environ. Earth Sci.* 74, 6459–6469.
- Wunch, D., Toon, G.C., Blavier, J.L., Washenfelder, R.A., Notholt, J., Connor, B.J., Griffith, D.W.T., Sherlock, V., Wennberg, P.O., 2011. The total carbon column observing network. *Philos. Trans. R. Soc.* 369, 2087–2112.
- Yoshida, Y., Kikuchi, N., Yokota, T., 2012. On-orbit radiometric calibration of SWIR bands of TANSO-FTS onboard GOSAT. *Atmos. Meas. Tech.* 5, 2515–2523.
- Yoshida, Y., Kikuchi, N., Morino, I., Uchino, O., Oshchepkov, S., Bril, A., Saeki, T., Schutzgens, N., Toon, G.C., Wunch, D., Roehl, C.M., Wennberg, P.O., Griffith, Q.W.T., Deutscher, N.M., Warnek, T., Notholt, J., Robinson, J., Sherlock, V., Connor, B., Rettinger, M., Sussmann, R., Ahonen, P., Heikkinen, P., Kyro, E., Mendonca, J., Strong, K., Hase, F., Dohe, S., Yokota, T., 2013. Improvement of the retrieval algorithm for GOSAT SWIR XCO₂ and XCH₄ and their validation using TCCON data. *Atmos. Meas. Tech.* 6, 1533–1547.
- Yoshida, Y., Ota, Y., Eguchi, N., Kikuchi, N., Nobuta, K., Tran, H., Morino, I., Yokota, T., 2011. Retrieval algorithm for CO₂ and CH₄ column abundances from short-wavelength infrared spectral observations by the greenhouse gases observing satellite. *Atmos. Meas. Tech.* 4, 717–734.
- Yue, T.X., 2011. *Surface Modelling: High Accuracy and High Speed Methods*. CRC Press, Boca Raton, FL.
- Yue, T.X., Chen, C.F., Li, B.L., 2010a. An adaptive method of high accuracy surface modeling and its application to simulating elevation surfaces. *Trans. GIS* 14, 615–630.
- Yue, T.X., Song, D.J., Du, Z.P., Wang, W., 2010b. High-accuracy surface modelling and its application to DEM generation. *Int. J. Remote Sens.* 31, 2205–2226.
- Yue, T.X., Zhang, L.L., Zhao, M.W., Wang, Y.F., Wilson, J.P., 2016. Space- and ground-based CO₂ measurements: a review. *Sci. China Earth Sci.* 59 (11), 2089–2097.
- Yue, T.X., Zhang, L.L., Zhao, N., Zhao, M.W., Chen, C.F., Du, Z.P., Song, D.J., Fan, Z.M., Shi, W.J., Wang, S.H., Yan, C.Q., Li, Q.Q., Sun, X.F., Yang, H., Wilson, J.P., Xu, B., 2015. A review of recent developments in HASM. *Environ. Earth Sci.* 74, 6541–6549.
- Yue, T.X., Zhao, N., Ramsey, D., Wang, C.L., Fan, Z.M., Chen, C.F., Lu, Y.M., Li, B.L., 2013b. Climate change trend in China, with improved accuracy. *Clim. Chang.* 120, 137–151.
- Yue, T.X., Zhao, N., Yang, H., Song, Y.J., Du, Z.P., Fan, Z.M., Song, D.J., 2013a. The multi-grid method of high accuracy surface modelling and its validation. *Trans. GIS* 17, 943–952.
- Zhang, L.L., Yue, T.X., Wilson, J.P., Wang, D.Y., Zhao, N., Liu, Y., Liu, D.D., Du, Z.P., Wang, Y.F., Lin, C., Zheng, Y.Q., Guo, J.H., 2016. Modelling of XCO₂ surfaces based on flight test of TanSat instruments. *Sensors* 16 (11), 1818.
- Zhao, M.W., Zhang, X.Y., Yue, T.X., Wang, C., Jiang, L., Sun, J.L., 2017. A high-accuracy method for simulating the XCO₂ global distribution using GOSAT retrieval data. *Sci. China Earth Sci.* 60 (1), 143–155.